




Evaporation of Leidenfrost droplet on thin soluble liquid bath with thermal non-equilibrium effect

Cite as: Phys. Fluids **34**, 093320 (2022); <https://doi.org/10.1063/5.0108939>

Submitted: 11 July 2022 • Accepted: 03 September 2022 • Accepted Manuscript Online: 06 September 2022 • Published Online: 26 September 2022

 Hao Wang (王浩),  Jinliang Xu (徐进良),  Xiaojing Ma (马晓婧), et al.



View Online



Export Citation



CrossMark

ARTICLES YOU MAY BE INTERESTED IN

[Suppression of Leidenfrost effect on superhydrophobic surfaces](#)

Physics of Fluids **33**, 122104 (2021); <https://doi.org/10.1063/5.0064040>

[Explosive boiling induced fast transportation of Leidenfrost droplet to target location](#)

Physics of Fluids **34**, 053322 (2022); <https://doi.org/10.1063/5.0091303>

[Splitting dynamics of droplet impact on ridged superhydrophobic surfaces](#)

Physics of Fluids **34**, 092104 (2022); <https://doi.org/10.1063/5.0105634>

Physics of Fluids

Special Topic: Hydrogen Flame and Detonation Physics

Submit Today!



Evaporation of Leidenfrost droplet on thin soluble liquid bath with thermal non-equilibrium effect

Cite as: Phys. Fluids **34**, 093320 (2022); doi: 10.1063/5.0108939

Submitted: 11 July 2022 · Accepted: 3 September 2022 ·

Published Online: 26 September 2022



View Online



Export Citation



CrossMark

Hao Wang (王浩),¹  Jinliang Xu (徐进良),^{1,2,a)}  Xiaojing Ma (马骁婧),^{1,2}  and Jian Xie (谢剑)^{1,2} 

AFFILIATIONS

¹Beijing Key Laboratory of Multiphase Flow and Heat Transfer for Low Grade Energy Utilization, North China Electric Power University, Beijing 102206, People's Republic of China

²Key Laboratory of Power Station Energy Transfer Conversion and System, North China Electric Power University, Ministry of Education, Beijing 102206, People's Republic of China

^{a)} Author to whom correspondence should be addressed: xjl@ncepu.edu.cn

ABSTRACT

Leidenfrost droplet evaporation on a liquid bath exhibits unique features such as ultra-low resistance to sample transition and low-temperature operation; however, the physical mechanisms responsible for these phenomena are incompletely understood. Droplet size and temperature are two key parameters influencing Leidenfrost droplet evaporation. We report herein the thermal non-equilibrium process of an FC-72 droplet over a thin oil layer. We show that the Leidenfrost droplet radius follows the power law $R(t) \sim (1 - t/\tau)^n$, where τ is the characteristic droplet lifetime and n ranges from 0.63 to 0.91. Based on experimental results and theoretical predictions, the remarkable nonmonotonic variation of droplet temperature departs from the saturation-temperature assumption. For lower oil superheating, a cold (subcooled) droplet can sustain evaporation until it disappears. For higher oil superheating, the droplet goes through both subcooled and superheating stages. This phenomenon is well described by sensible heat absorption and release throughout droplet evaporation. These results are helpful for applications such as drug delivery, wherein a cold droplet can float on a liquid bath, thereby extending the lifetime of the biological sample in a high-temperature environment via a localized, low-temperature system.

Published under an exclusive license by AIP Publishing. <https://doi.org/10.1063/5.0108939>

I. INTRODUCTION

Droplet or bubble dynamics on a soft surface (solid or liquid) invites new applications such as enhanced heat transfer and droplet manipulation.^{1–3} Leidenfrost droplets have a wide range of applications in drug-delivery,⁴ and nanofabrication,^{5,6} due to their self-propelling behavior^{7,8} and chemical reaction characteristics.⁹ In contrast to the widely studied Leidenfrost droplet evaporation on a rigid surface, a liquid surface is extremely smooth, which lowers the temperature for forming a Leidenfrost droplet and increases the droplet radius. For droplet evaporation floating on a liquid bath, the temperature field of the liquid bath may alter the heat transfer from the liquid bath to the droplet.¹⁰ The external environment may disturb the liquid bath to influence the thickness and shape of the vapor film beneath the droplet.¹¹ The Rayleigh–Taylor instability at the droplet interface causes the symmetry breaking of the droplet to affect the droplet evaporation.¹² Hence, Leidenfrost droplet evaporation on a liquid bath is complicated due to the coupling of mass, momentum, and energy transfer in the liquid bath, the presence of a vapor film below the droplet, and the droplet itself and its environment.

Droplet size and temperature are two key parameters in droplet dynamics. Because different forces scale differently with respect to droplet size, droplet radius is a crucial factor in the force balance and dominates the physics when a droplet is levitated over a liquid bath. If the force balance is broken, a Leidenfrost droplet either jumps^{13,14} or triggers direct contact boiling.^{15,16} A net force applied on a droplet causes droplet acceleration, which may be used for droplet self-propulsion.^{17–20} On the other hand, droplet temperature dominates the temperature difference that governs the rate of heat transfer between the liquid bath and the droplet and influences the Marangoni flow intensity inside the droplet.^{21,22} In the upper region of the droplet, the droplet temperature affects the vapor pressure at the gas–liquid interface, influencing vapor diffusion from the droplet to the environment.²³

Leidenfrost droplets on solid surfaces have been widely studied. Quéré¹² and Ajaev and Kabov²⁴ commented on Leidenfrost droplets. Assuming pure conductive heat transfer across the vapor film and a lubrication flow in the vapor film, Biance *et al.*²⁵ showed that the Leidenfrost droplet radius on a solid wall should follow the power law

$R(t) = R_{\text{ini}}(1 - t/\tau)^n$, where R is the radius projected by the droplet on the substrate, R_{ini} is the initial droplet radius, and n is an exponent that depends on the droplet shape, where $n = 2$ for a droplet with a radius larger than the capillary length and having a puddle shape and $n = 0.5$ for a quasi-spherical droplet with a radius smaller than the capillary length.²⁵ Maquet *et al.*²⁶ studied Leidenfrost droplets of ethanol on silicon–oil surface with an oil viscosity $\mu_o = 0.202$ Pa s, an initial droplet radius $R_{\text{ini}} = 0.9$ mm, and an oil superheating ΔT_{sat} in the range 3–92 °C ($\Delta T_{\text{sat}} = T_o - T_{\text{sat}}$, where T_o and T_{sat} are the oil surface temperature and the saturation temperature of the droplet, respectively). Maquet *et al.* proposed that $R(t) \sim (1 - t/\tau)^n$ is valid with $n = 1$.²⁶

The Leidenfrost droplet temperature is usually assumed to be the saturation temperature corresponding to the pressure exerted by the environment.^{26–29} However, this hypothesis is not supported by experimental measurements. Orzechowski and Wcislik³⁰ monitored the temperature of large water droplets $\{R \approx 0.8 \text{ cm} \gg l$, where $l = [\sigma/(\rho g)]^{1/2}$ is the capillary length of water} floating on a hot solid surface. The difference between the maximum and minimum temperatures periodically exceeded 9 °C, and the standard deviation in the temperature of the area covering about 80% was substantial (2 °C).³⁰ Yim *et al.*³¹ investigated droplet temperatures and reported that the internal droplet temperature is very uniform at about 80 °C for small droplets of radius $R < l$, which is significantly lower than the water saturation temperature of 100 °C. Mogilevskiy³² investigated non-boiling droplets over a hot liquid bath and reported that droplet temperatures evolve in three stages with respect to time (rise, constant, rise). Castanet *et al.*³³ investigated water droplets impacting a sapphire wall heated to a temperature ranging from 300 °C to 700 °C, causing significant droplet overheating. Under extreme conditions, droplets can reach temperatures of several hundred degrees, which triggers homogeneous boiling in droplets.³³ Therefore, for Leidenfrost droplet evaporation, the droplet temperatures may be changed vs time,^{30,32} or deviating from the saturation temperature.^{31,33}

For Leidenfrost droplet evaporation, the connection between droplet sizes and temperatures is not reported in the literature. Physically, assuming droplet evaporation in air environment, smaller droplet has larger surface to volume ratio, promoting an heat/mass transfer from droplet to environment to approach the saturation state of the droplet. On the contrary, larger droplet may deviate from the saturation temperature. Except the effect of droplet sizes on temperatures, many factors influence droplet temperatures. For droplet exposed in air, a vapor boundary layer exists close to the droplet surface.³⁴ Vapor diffusion dominates the evaporation mass flux from droplet to environment.³⁵ Hence, the temperature and humidity of air influence the mass transfer thus to affect the droplet temperature.^{34,36} It is reported that environment pressure influences the evaporation rate of droplet.³⁷ Under high temperature environment, evaporation becomes faster when increasing pressures.³⁷ Inside the droplet, the Marangoni number Ma is scaled to the drop radius R as $Ma \sim R^{-2}$.³⁶ Thus, drop size influences Ma to dominate the internal circulation to influence the temperature uniformity of the droplet. For evaporation of sessile droplet on rigid surface, roughness and wettability of the wall surface influence the heat and mass transfer of the droplet,^{38,39} which are beyond the scope of the present paper.

The present paper focusses on the investigation of transient droplet sizes and temperatures. This paper consists of two parts: The first

part focuses on measuring transient droplet size. Using the power-law assumption of droplet size, we determine the power exponent at different oil superheating. The second part proposes an analytical model to predict the transient droplet temperature. Given the experimentally determined exponent and characteristic droplet lifetime, the droplet temperature can be determined, and the results are consistent with the measured values. Both experiments and predictions indicate that the droplet is far from thermal equilibrium during the entire time that the droplet resides on the surface of the liquid bath.

II. MATERIALS AND METHODS

Figures 1(a) and 1(b) show the experimental setup, which consists of a needle for droplet release, an infrared (IR) camera, a copper block with a $10 \times 6 \times 2 \text{ mm}^3$ rectangular slot to store the oil, and a power-control system. The slot was filled with dimethyl silicon oil (XIAMETER PMX-200), keeping the oil surface slightly below the upper copper surface. Three oil samples were used with viscosities of $\mu_o = 0.048, 0.097, \text{ and } 0.485$ Pa s (see Table I for the physical properties of dimethyl silicon oil). The temperature of the copper block was controlled by a heating system, which consisted of two cartridge heaters rated at 30 W, two embedded thermocouples, and an external temperature control device. The proportional-integral-derivative control system ensured that fluctuations in the copper block temperature were less than 0.5 °C. The control system uses the integration and differentiation logic to control the temperature of the copper block; thus, the oil temperature can be controlled. By setting a desired temperature, if the real temperature of the copper block is below the desired temperature by a specific amount such as 0.2 °C, the heater is turned on. Otherwise, if the real temperature is above the desired temperature by a specific amount such as 0.2 °C, the heater is turned off. In such a way, the copper block is controlled to be the desired temperature by a small amount of variation.

Driven by a micro-pump, an FC-72 (3 MTM FluorinertTM Electronic Liquid) droplet was ejected from a needle approximately 2.5 mm above the upper copper surface. The droplet volume was $1.77 \pm 0.03 \mu\text{L}$, corresponding to a drop radius $R_{\text{ini}} = 0.75$ mm. One notes that the droplet size can be varied from case to case. However, all the tests covered the drop radius within (0.75 ± 0.1) mm. For droplet impacting a surface, the Weber number $We = \rho v^2 D_{\text{ini}} / \sigma$ quantifies the importance of kinetic energy relative to surface energy, where ρ , σ , v , and D_{ini} are the density, surface tension, incident velocity, and initial droplet diameter, respectively. The Weber number influences the dynamics and the temperatures of droplets.^{40,41} For high We such as $6 < We < 600$, the droplet impacting involves the spreading and receding processes, thus the impacting characteristic time is increased.⁴² In the present study, the We number is 7.2, ensuring that the impacting does not contain the spreading and receding processes. In such a way, droplet dynamics is less influenced by the impacting height for low We number cases.

At atmospheric pressure, an FC-72 droplet has a surface tension of $\sigma_1 = 0.014$ N/m and a liquid density of $\rho_1 = 1680 \text{ kg/m}^3$, which is heavier than silicon oil ($\approx 1000 \text{ kg/m}^3$, see Table I for the physical properties of silicon oil and FC-72 droplets). The FC-72 droplet is soluble in silicon oil. Because $R_{\text{ini}} \approx 0.75$ mm is less than the FC-72 capillary length $l = [\sigma_1/(\rho_1 g)]^{1/2} = 0.92$ mm, where g is the acceleration due to gravity on Earth, the droplet is quasi-spherical. Heating by the oil surface causes droplet evaporation, which decreases the droplet size,

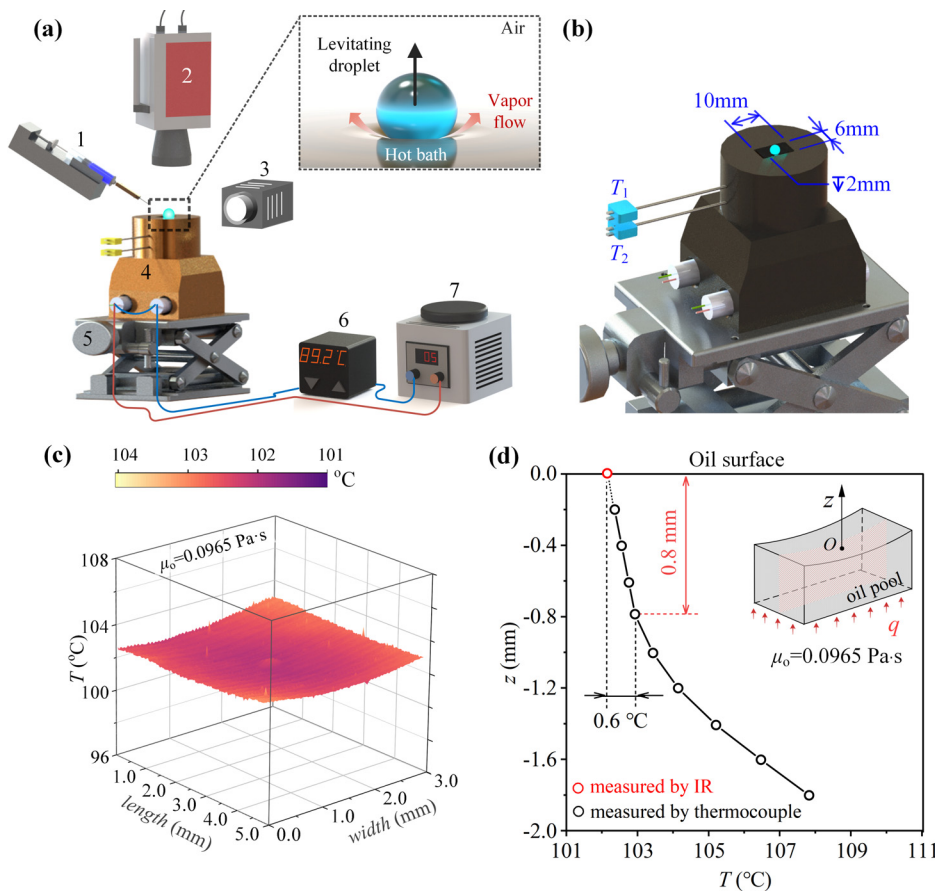


FIG. 1. Experiment setup and measurement. (a) 3D drawing for experiment setup and IR measurement: (1) needle for droplet release, (2) IR camera, (3) high-speed camera, (4) copper block, (5) displacement adjustment platform, (6) proportional-integral-derivative temperature controller, and (7) voltage transformer. (b) Copper block with the microchannel slot to store liquid. (c) Temperature field on the silicon oil surface. (d) Temperature distribution in the oil depth direction.

making it difficult to separate the droplet from the needle. Therefore, a micro-heat-exchanger was mounted at the needle tip to compensate for this heating effect by suppressing the temperature rise of the droplet before its separation from the needle. The oil superheating temperature difference, which is defined as the oil temperature minus the saturation temperature of FC-72, covers the range 14–69 °C.

As shown in Fig. 1(b), the rectangular slot has a size of 10 mm in length, 6 mm in width, and 2 mm in depth. During experiment, silicon oil is filled in the slot with the oil depth slightly smaller than the slot

depth. Compared to deep liquid pool, the shallow depth of the slot ensures larger ratio of the surface area for copper–oil contact to the slot volume, keeping relatively uniform oil temperature in the slot. The shallow oil depth also limits the intensities of natural convection and Marangoni flow in the oil. Because copper is oleophilic, the oil surface is concave, which is beneficial to locate a droplet in the slot. For Leidenfrost evaporation, the droplet always finds the center and lowest position of the oil surface, minimizing the disturbance caused by droplet motion above the oil surface.

TABLE I. Physical properties of FC-72 and silicon oil under reference conditions ($P = 1 \text{ atm}$).

	FC-72 (25 °C)		Silicone oil #1(20 °C)	Silicone oil #2(20 °C)	Silicone oil #3(20 °C)
	Liquid	Vapor			
$\rho \text{ (kg m}^{-3}\text{)}$	1680	9.718	960	965	970
$T_{\text{sat}} \text{ (}^\circ\text{C)}$	56.6	×	×	×	×
$c_p \text{ (J kg}^{-1} \text{K}^{-1}\text{)}$	1100	900	×	×	×
$\mu \text{ (kg m}^{-1} \text{s}^{-1}\text{)}$	6.4×10^{-4}	1.31×10^{-6}	0.048	0.0965	0.485
$\sigma \text{ (N m}^{-1}\text{)}$	0.014	×	0.0208	0.0209	0.0212
$d\sigma/dT \text{ (N m}^{-1} \text{K}^{-1}\text{)}$	0.09811	×	6×10^{-5}	6×10^{-5}	6×10^{-5}
$L \text{ (J kg}^{-1}\text{)}$	8.81×10^4	×	×	×	×

The oil surface temperature is measured by an IR camera (InfrTec, ImageIR 5380), and the temperatures in the oil depth direction are measured by thermocouples [see Figs. 1(c) and 1(d)]. The IR camera captures the temperature with a wavelength of 3–5 μm band and a spatial resolution of 12.4 μm . The temperature sensitivity is 0.02 $^{\circ}\text{C}$. A measurement case is shown in Fig. 1(c). The temperature difference across the entire focusing area ($3 \times 5 \text{ mm}^2$) of the IR camera was less than 0.5 $^{\circ}\text{C}$, while the oil surface temperature was above 100 $^{\circ}\text{C}$. For the measurement in the oil depth direction, an original point O is defined at the center surface of the oil, and a z coordinate is defined toward the upward direction. The temperature curve in the depth direction is measured by a thermocouple. As shown in Fig. 1(d), the oil surface temperature T_o is 102 $^{\circ}\text{C}$ by the IR measurement, dotted by the red color. This temperature well matched by the value at $z=0$ extended from the measured curve in the depth direction by thermocouples, dotted by black color, noting that the uncertainty of thermocouples is 0.1 $^{\circ}\text{C}$. This validation ensures the precise measurement of the oil surface temperatures. The temperature difference is 0.6 $^{\circ}\text{C}$ from the oil surface to a depth of 0.8 mm [see Fig. 1(d)].

Our experiment involved measuring the temperature of both the silicon oil and the FC-72 droplet by the IR camera. The system was carefully calibrated before the experiment. A 10-mm-outer-diameter test tube stored either FC-72 or silicon oil [see Fig. 2(a)]. The test tube was immersed in a larger oil bath, which was held at the desired temperature to within 0.2 $^{\circ}\text{C}$. Given sufficient time, the oil bath reached thermal equilibrium with the liquid in the test tube at which point the

surface temperature of the liquid in the test tube was measured by both the IR camera and a precision thermocouple. The latter was immersed 0.5 mm into the liquid and had an accuracy of 0.1 $^{\circ}\text{C}$. The temperature measured by the thermocouple correlated linearly with that measured by the IR camera with correlation coefficients of 0.9964 for FC-72 and 0.9999 for silicon oil [see Figs. 2(b) and 2(c)].

Transient droplet temperature and size are two key parameters in this work. In the central region of the droplet, the droplet penetration length h_b was sufficient and exceeded the critical optical length L_c , ensuring a precise measurement of the temperature [see Fig. 3(a)]. Figures 3(b) and 3(c) show the temperature acquired by a top-view measurement by the IR camera. The figures show a central droplet region, a thin boundary layer δ_b , and an oil region. Temperatures were flattened in the droplet region, but increased sharply upon entering the boundary-layer region until a higher temperature was attained in the oil region. The point at which the temperature started rising sharply is defined as the boundary of the precise temperature measurement. Inside the droplet, the temperature difference is less than 1 $^{\circ}\text{C}$ [see Figs. 3(b) and 3(c)]. For all the tests, droplet temperature can be regarded as uniform, due to the smaller Biot number 0.016. This treatment is like those of Refs. 25–29. Classically, a body can have a uniform temperature when the Biot number is less than 0.03.⁴⁵ The droplet temperature T_d is defined as the average value over the central region of the droplet.

To determine the droplet diameter based on the temperature as measured by the IR camera, one needs to know the droplet margin

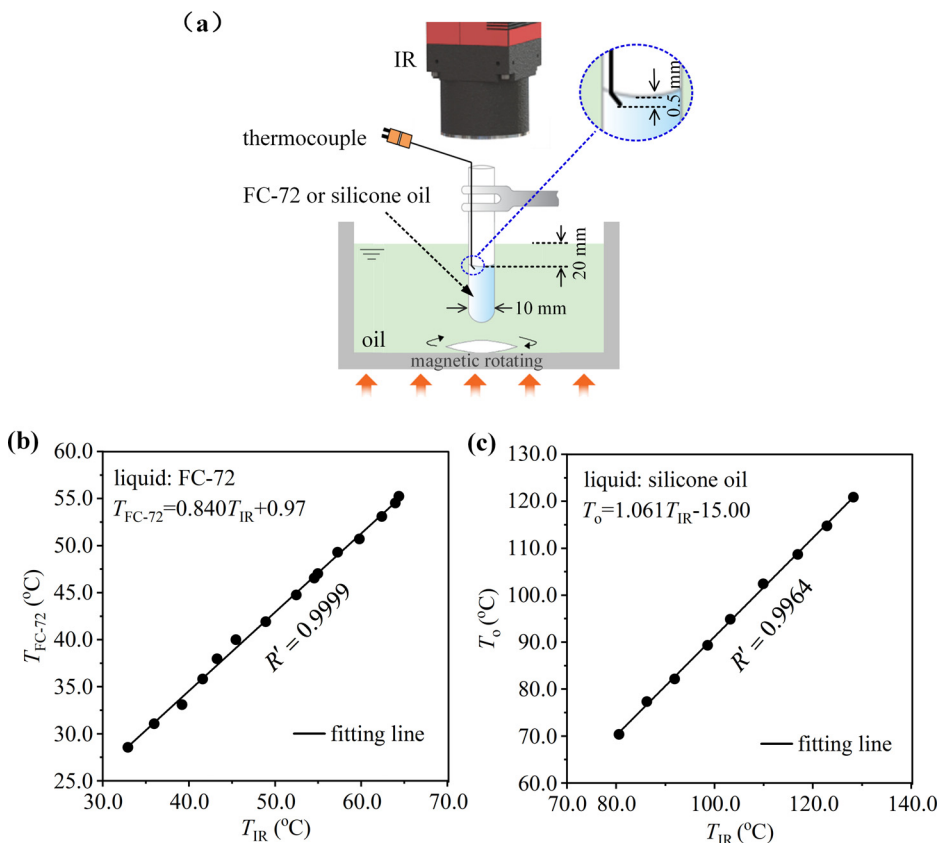


FIG. 2. Calibration of surface temperature measurement for silicon oil and FC-72. T_{IR} is the temperature measured by the IR camera, $T_{\text{FC-72}}$ and T_o are the temperatures measured by a standard thermocouple. (a) Experiment setup for the calibration. (b) Calibration line for FC-72. (c) Calibration line for silicon oil.

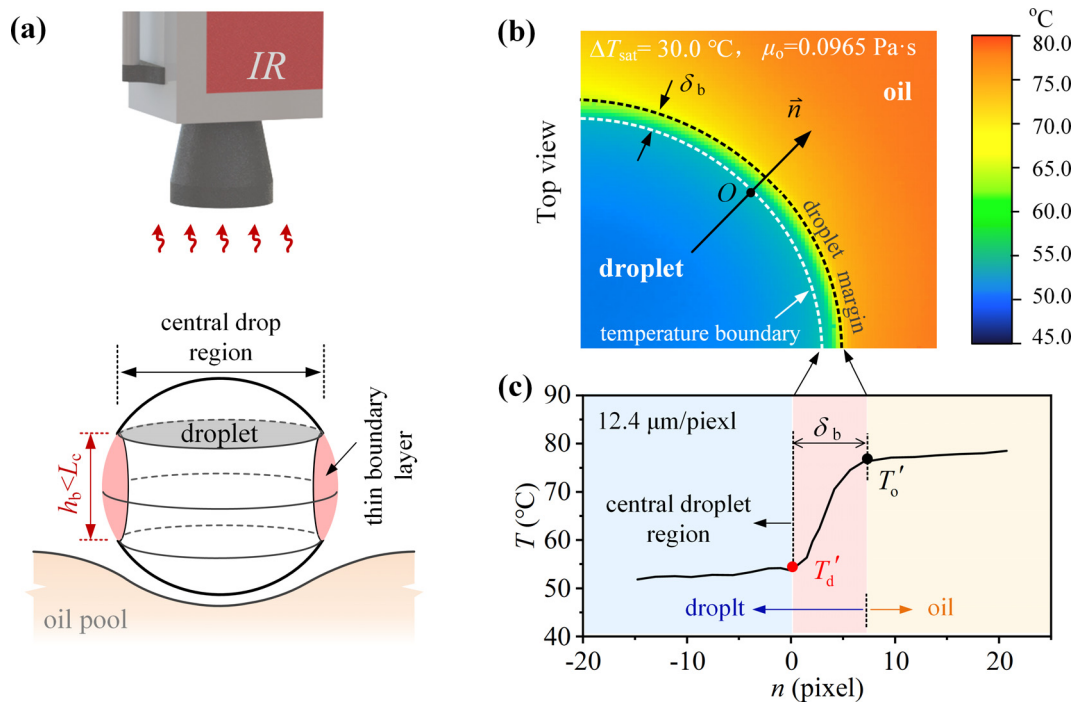


FIG. 3. The principle to locate the drop interface by the IR measurement. (a) The principle. (b) IR measured temperature (planar view). (c) Measurement outcome in which three regions of droplet body, temperature boundary, and oil is divided.

(T'_o), which is regarded as the transition point from the boundary-layer region to the oil region [see Figs. 3(b) and 3(c) for a top view]. For measuring the drop size, a droplet diameter of approximately 1 mm produces very little uncertainty. An initial diameter $D_{ini} \approx 1.5$ mm has an uncertainty of 0.8% with respect to the $12.4 \mu\text{m}$ spatial resolution obtained from the IR camera, and this error increases with decreasing droplet size. Later, we show that an FC-72 Leidenfrost droplet explodes when its diameter reaches $D \approx 0.2D_{ini}$, at which point the relative error in the measured droplet size is 4.1%. Thus, both droplet diameter and temperature are precisely determined. The experiment was done at $25 \pm 2^\circ\text{C}$ and at a relative humidity of about 30%. Table II lists instruments used in this study and uncertainties of various parameters, including temperatures, droplet sizes, and time. These parameters are directly measured by instruments. The vapor film thickness δ is theoretically predicted. As seen from Eq. (15), δ is a

function of $R(t)$, T_o and T_d : $\delta = f(R(t), T_o, T_d)$. Based on the error transmission principle,⁴⁶ the uncertainty of δ can be evaluated as follows:

$$\Delta\delta = \sqrt{\left(\frac{\partial\delta}{\partial R(t)}\Delta R(t)\right)^2 + \left(\frac{\partial\delta}{\partial T_o}\Delta T_o\right)^2 + \left(\frac{\partial\delta}{\partial T_d}\Delta T_d\right)^2}. \quad (1)$$

Based on the measurement of R , T_o , and T_d and their uncertainties, we achieve the relative error of δ is 9.89% (maximum value).

III. RESULTS AND DISCUSSION

A. Transient droplet size and temperature

We present the size of droplets levitating on an oil surface. The experiments are characterized by the oil superheating temperature difference $\Delta T_{sat} = T_o - T_{sat}$, where T_o and T_{sat} are the oil surface

TABLE II. Instruments and uncertainties of various parameters.

Parameters	Parameter range	Instruments	Uncertainties
Temperature	10–108 °C	Micro-thermocouple	0.1 °C
Oil temperature (T_o)	70–127 °C	IR (InfrTec, ImageIR 5380)	0.02 °C
Droplet temperature (T_d)	20–65 °C	IR (InfrTec, ImageIR 5380)	0.02 °C
Droplet radius (R)	0–0.75 mm	IR (InfrTec, ImageIR 5380)	12.4 μm
Droplet radius (R)	0–0.75 mm	High-speed camera (VW-9000)	4.7 μm
Time (t)	×	MotionPro Timing Hub	0.05 s
Film thickness (δ)	×	×	2.98–9.89%

temperature and the saturation temperature of the droplet, respectively. In this work, ΔT_{sat} falls in the range 14–69 °C. Given that the droplets are quasi-spherical, the drop size visualized by the high-speed camera (side view) is essentially the same as that obtained by the IR camera (top view). For small ΔT_{sat} , the deposited droplet quickly sinks and dissolves into the oil, which is called “droplet sinking” and lasts approximately 2 s [see Fig. 4(a)]. When a droplet approaches the oil surface, an air film forms between the droplet and the oil. A slight delay occurs as the gas is removed from the thin gap between droplet and oil, after which the droplet and oil come into direct contact, which triggers sinking. Zawala *et al.*⁴⁷ label this process “film drainage.”

With increasing ΔT_{sat} , a critical oil temperature triggers Leidenfrost evaporation with a much longer residence time ($\tau_r \approx 10$ s). In the later stage of evaporation, smaller droplets suddenly explode, which is explained by the unbalanced force induced by contact boiling, after which the oil surface gradually flattens [see Fig. 4(b)]. For a levitated droplet, the gravity force should be balanced by the lifting force $P \sim R^2$ due to vapor pressure in thin vapor film, where R is the droplet

radius. Considering the vapor film, the lifting force should be balanced by the capillary force $F_\sigma \sim R$ due to deformation of the oil surface. Thus, the scaling $P/F_\sigma \sim R$ is derived. A critical value exists due to the competition between these two forces. When P/F_σ is less than the critical value, contact boiling between droplet and oil occurs because the vapor pressure in the vapor film is insufficient to resist the surface-deformation-induced capillary force.^{48,49} Such later-stage explosions of Leidenfrost droplets were also reported by Lyu *et al.*⁵⁰

Figure 4(c) indicates that increasing oil viscosity shifts the residence time curve to the right (i.e., to longer times). The Leidenfrost transition temperature increases with increasing oil viscosity, which is similar to the transition temperature, which increases with increasing wall roughness for Leidenfrost droplets on a solid wall.⁵¹ Apparently, a higher oil viscosity slows the evaporation. However, our analysis indicates that the different residence times τ_r shown in Fig. 4(c) are caused by different surface tensions of the three oil samples, instead of different viscosities. Note that heat transfer from oil to droplet across a

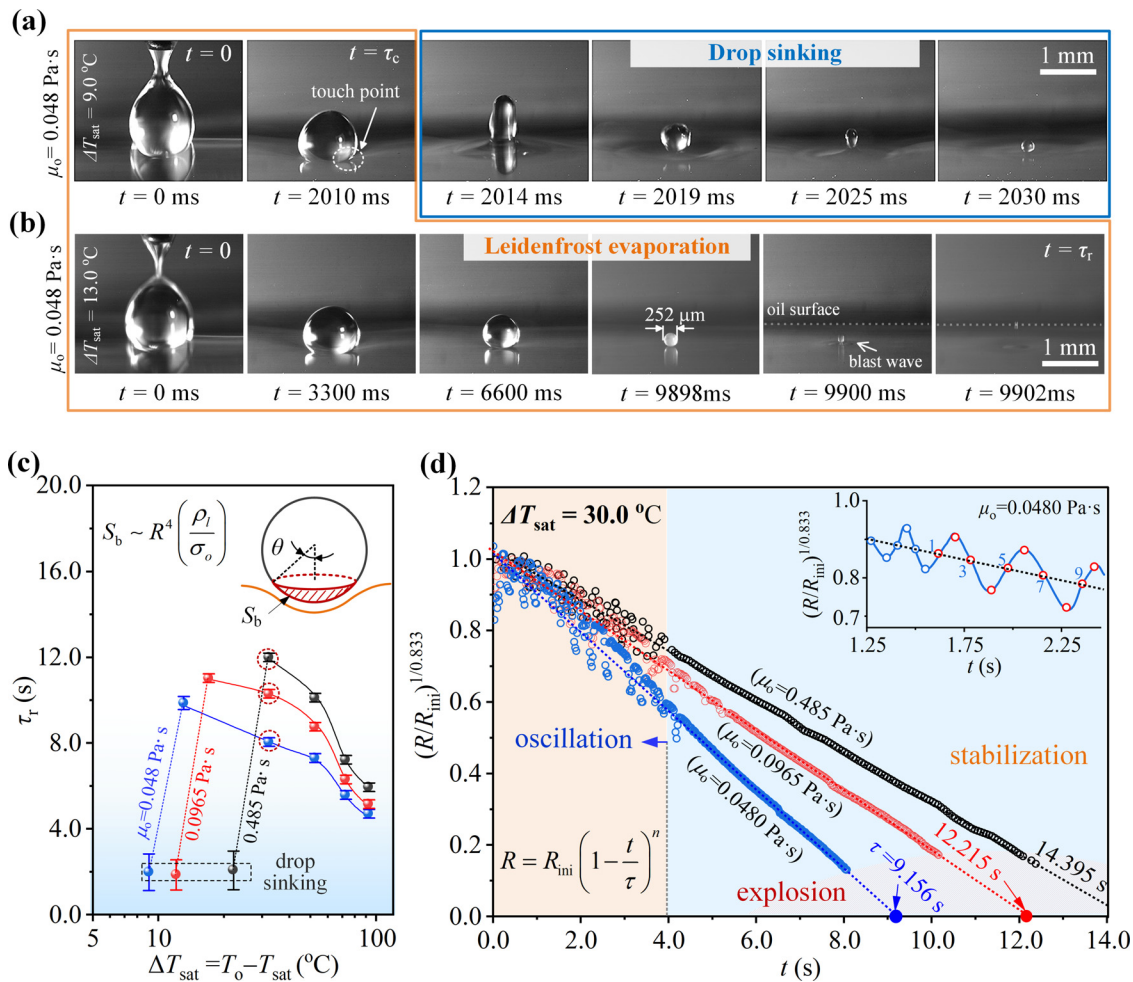


FIG. 4. Droplet dynamics. (a) Drop sinking mode, (b) Leidenfrost mode, and (c) residence time τ_r of an FC-72 droplet with radius $R_{\text{ini}} = 0.75$ mm as a function of oil superheating ΔT_{sat} . (d) Linear correlation of $(R/R_{\text{ini}})^{1/n} \sim t$ (illustration shows drop oscillating in the initial stage). Multimedia view: <https://doi.org/10.1063/5.0108939.1>

curved surface of area $S_b = 2\pi R^2(1 - \cos \theta)$, where θ is the half-angle of the taper facing the oil surface [see illustration in Fig. 4(c)]. The force balance between gravity acting on the droplet and surface tension of the oil surface yields $\theta = R [2\rho_l/(3\sigma_o)]^{1/2}$, where R is the droplet radius and σ_o is the surface tension of the oil. Substituting this angle into S_b yields $S_b \sim R^4(\rho_l/\sigma_o)$. Of the three oil samples, the sample with $\mu_o = 0.485$ Pa s has the largest surface tension $\sigma_o = 21.2$ mN/m, so this oil sample has the smallest surface area S_b for heat transfer, which slows the evaporation process.

Figure 4(d) (Multimedia view) shows the normalized transient droplet radius $R(t)/R_{ini}$, which goes through three stages: oscillating, steady state, and explosion. In the early stage with $[R(t)/R_{ini}]^{1/0.833}$ [where 0.833 is the experimentally determined exponent; see Eq. (2)] ranging from 1 to 0.56 for $\mu_o = 0.0480$ Pa s, from 1 to 0.69 for $\mu_o = 0.0965$ Pa s, and from 1 to 0.74 for $\mu_o = 0.485$ Pa s, the droplet sizes decrease during the oscillation because of the competition between gravity and the capillary force. Gravity tends to deform the droplet and lower its center of mass, whereas the capillary force tends to maintain the spherical shape to minimize the droplet surface energy. The largest oscillating amplitude is less than 8% [see illustration in Fig. 4(d)].

To explore the variation in droplet size, the characteristic droplet lifetime τ is introduced except τ_r . Assuming no explosive boiling, τ is obtained by extending the fit of $R(t)/R_{ini}$ to $R = 0$ at $t = \tau$ [see Fig. 4(d)]. In this case, $\tau > \tau_r$. For example, with

$\Delta T_{sat} = 30.0^\circ\text{C}$ and $\mu_o = 0.0965$ Pa s, $\tau = 12.2$ s, which is longer than $\tau_r = 10.2$ s. The three stages of the phenomenon are presented in Fig. 5 and include an early stage droplet expansion and shrinking, a continuous steady evaporation, and a later explosion-induced blast wave lasting 24 ms, which is three orders of magnitude less than the residence time τ_r .

The power-law correlation gives the following equation for $\Delta T_{sat} = 30.0^\circ\text{C}$:

$$\frac{R(t)}{R_{ini}} = \left(1 - \frac{t}{\tau}\right)^{0.833}, \quad (2)$$

where $n = 0.833$ is the experimentally determined exponent.

Figure 6(a) shows how ΔT_{sat} affects variation of droplet sizes: n decreases with increasing ΔT_{sat} . With ΔT_{sat} in the range $14\text{--}69^\circ\text{C}$, n covers the range 0.91–0.63. Increased superheating increases the temperature difference between oil and droplet. Figure 6(b) shows the temperature difference $T_o - T_d$ during the droplet residence time. Three curves are presented with three different oil superheating temperature differences. The temperature difference $T_o - T_d$ differs from the oil superheating temperature difference ΔT_{sat} . For $\Delta T_{sat} = 14.8^\circ\text{C}$, the droplet is always subcooled, so $T_o - T_d > \Delta T_{sat}$. On the contrary, $T_o - T_d$ can be greater or less than ΔT_{sat} because the droplet goes through a subcooled stage and a superheating stage. Later, we further discuss how oil superheating causes the droplet temperature to deviate

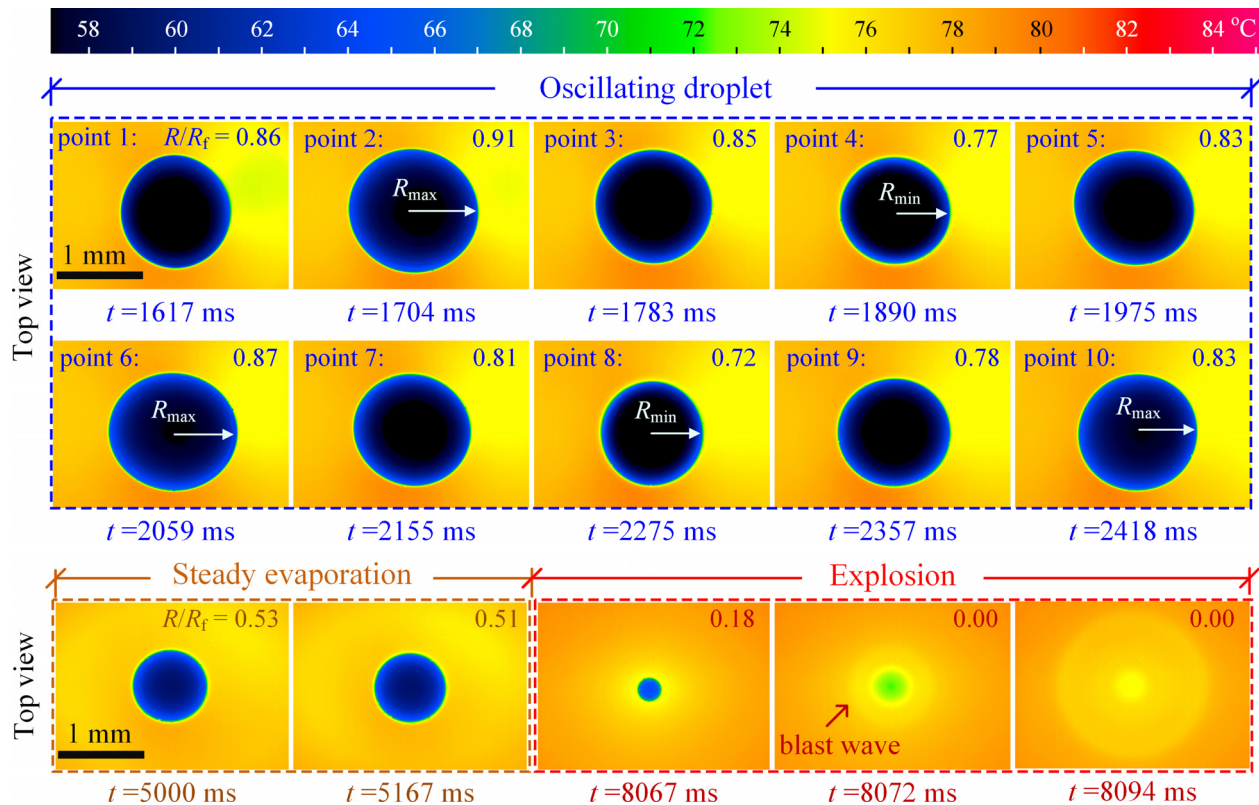


FIG. 5. IR image files showing the three stages of oscillating evaporation, steady evaporation, and explosion with $\mu_o = 0.048$ Pa s.

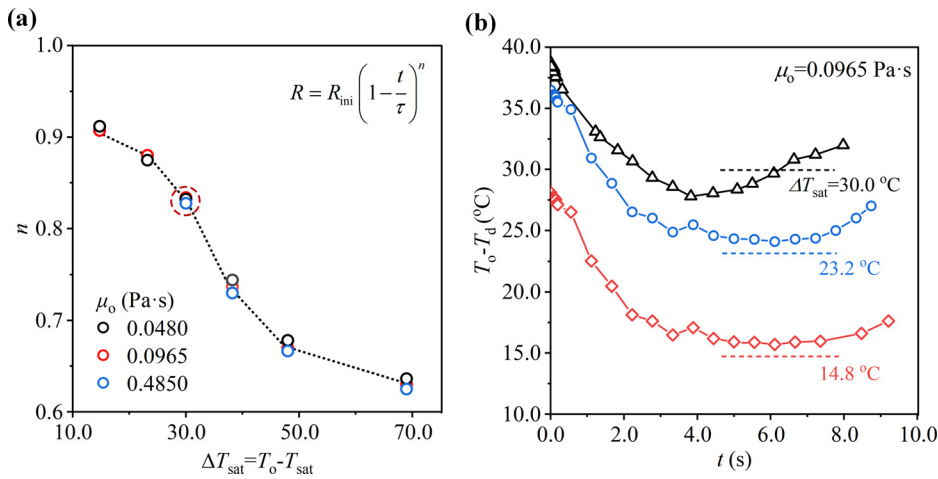


FIG. 6. Variation of droplet size and temperatures. (a) Power exponent n influenced by oil superheating and viscosities. (b) Transient temperature difference $T_o - T_d$ between oil and droplet as a function of time for three oil superheating degrees.

from the saturation temperature and how it influences mass transfer in the upper-droplet region.

B. Theoretical model for droplet dynamics

Previous studies assume the saturation temperature of droplet and neglect diffusion-controlled mass transfer in the upper-droplet region, thereby underpredicting the droplet evaporation rate, especially for small droplets with $R < l$.^{25,52} Here, to predict droplet dynamics, a modified model is proposed that considers diffusion-controlled mass transfer in the upper-droplet region. The model consists of two parts, with the first part dealing with the vapor-layer thickness and the second part dealing with energy conservation within the droplet. The two parts are coupled to predict the droplet temperature given the input parameters of characteristic lifetime τ and power exponent n .

The analysis of δ involves two steps: In the first step, we analyze the force balance between droplet and vapor layer, and, in the second step, we analyze the force balance at the oil surface due to the curvature (see Fig. 7). At the oil surface, the thickness of the vapor film under a droplet is nearly uniform, which is unlike the dimple-shaped vapor film at a solid surface.^{26,29,53} In the vapor layer, the simplification of the Navier–Stokes equation and application of the lubrication theory yield the vapor velocity u_v as⁵⁴

$$u_v = \frac{1}{2\mu_v} \frac{dp}{dr} z(z - \delta), \tag{3}$$

where μ_v is the vapor viscosity, p is the pressure dependent on r , and z is the vertical coordinate, which has its origin at the oil surface. The average vapor velocity $u_{v,ave}$ is

$$u_{v,ave} = \frac{1}{\delta} \int_0^\delta u_v dz = -\frac{\delta^2}{12\mu_v} \frac{dp}{dr}. \tag{4}$$

Note the coefficient of 1/12 in the mobility factor, which is typical when no-slip conditions are imposed at both the droplet surface and oil interface.^{26,32,55} The volume flow rate $q_{v,b}$ due to evaporation in the vapor layer, having units of m^3/s , is

$$q_{v,b} = 2\pi\delta u_{v,ave} R \sin \theta = -\frac{\pi R \sin \theta \delta^3}{6\mu_v} \frac{dp}{dr}. \tag{5}$$

The ratio of $q_{v,b}$ relative to the total volume flow rate q_v is denoted $s(t)$ ²⁵ and the diffusion-controlled mass transfer in the upper-droplet region is given by

$$s(t) = \frac{q_{v,b}}{q_v} = \left(\frac{R_d}{R}\right)^2 = \sin^2 \theta, \tag{6}$$

where R_d is the maximum “contact” radius of the droplet above the oil surface and θ is the half-angle delimiting the vapor-layer region that

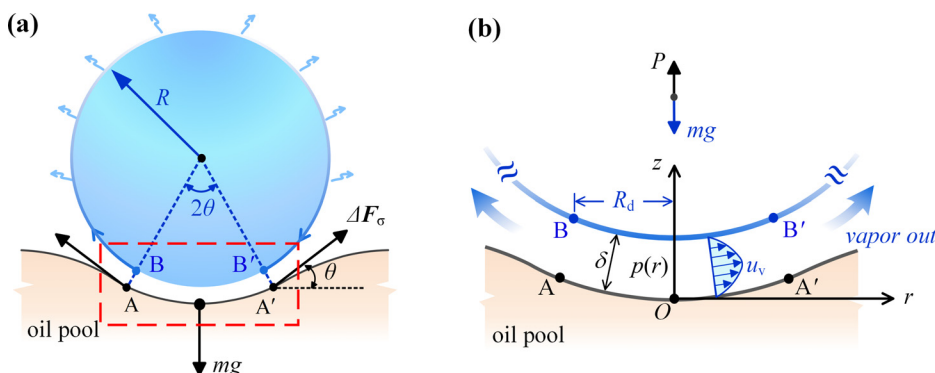


FIG. 7. Physical model for predicting vapor layer thickness. (a) The geometry of droplet floating on soft liquid, and (b) force analysis, velocity profile and parameters definition of the physical model.

ends at the separation points B and B' [see Fig. 7(a)]. Combining Eqs. (5) and (6) yields the pressure gradient in the radial direction,

$$\frac{dp}{dr} = -\frac{6\mu_v q_v \sin \theta}{\pi R \delta^3}. \tag{7}$$

Integrating Eq. (7) with respect to r and applying the boundary condition at $r = R_d$, $p = p_a$, where p_a is the air environment pressure, yields

$$p(r) - p_a = \frac{6q_v \mu_v \sin \theta}{\pi \delta^3} \left(\sin \theta - \frac{r}{R} \right). \tag{8}$$

Thus, the lifting force supplied by the vapor layer to levitate the droplet is obtained by integrating the component forces acting on the droplet in the vertical direction,

$$P = \int_0^{R_d} (p(r) - p_a) 2\pi r dr = \frac{2q_v \mu_v R^2 \sin^4 \theta}{\delta^3}. \tag{9}$$

Assuming that heat conduction across δ accounts for droplet evaporation, we have^{12,25,26,52}

$$-\lambda_v \frac{dT}{dz} S_b = -\rho_v q_v L, \tag{10}$$

where λ_v is the thermal conductivity of the vapor, S_b is the contact area between the droplet and the vapor layer, and ρ_v and L are the vapor density and the latent heat of evaporation, respectively. Substituting the boundary conditions $z = 0$, $T = T_o$, and $z = \delta$, $T = T_d(t)$ yields

$$q_v = \frac{2\pi R^2 \lambda_v [T_o - T_d(t)] (1 - \cos \theta)}{\delta(t) L \rho_v}. \tag{11}$$

Substituting q_v [Eq. (11)] into P [Eq. (9)] and balancing the forces P and gravity give

$$\delta(t) = \left(\frac{3R \lambda_v \mu_v [T_o - T_d(t)] (1 - \cos \theta) \sin^4 \theta}{L \rho_v \rho_l g} \right)^{1/4}. \tag{12}$$

Force balance on the curved oil surface is imposed to deduce θ (see Fig. 7),

$$2\pi \sigma_o R \sin^2 \theta = mg = \frac{4\pi}{3} R^3 \rho_l g. \tag{13}$$

Considering small θ and rewriting Eq. (13) yields

$$\sin \theta \approx \theta = \frac{R}{l_o} \sqrt{\frac{2\rho_l}{3\rho_o}}, \tag{14}$$

where $l_o = [\sigma_o/(\rho_o g)]^{1/2}$ is the capillary length of oil and ρ_l and ρ_o are the liquid densities of FC-72 and oil, respectively. Finally, the vapor-layer thickness is

$$\delta(t) = l_o^{-3/2} \left(\frac{2\rho_l}{3\rho_o} \right)^{3/4} \left(\frac{3\lambda_v \mu_v}{2L\rho_l \rho_v g} \right)^{1/4} R(t)^{7/4} [T_o - T_d(t)]^{1/4}. \tag{15}$$

To analyze the droplet temperature, the droplet sensible heat should be considered. Modifying the energy equation yields

$$-\lambda_v \frac{dT}{dz} S_b = \rho_v q_v L + \frac{d\{m c_{p,l} [T_d(t) - T_{ini}]\}}{dt}, \tag{16}$$

where T_{ini} is the initial droplet temperature and $c_{p,l}$ is the specific heat of FC-72. The second term of Eq. (16) represents the variation in sensible heat. Applying a similar treatment as given in Sec. III B for dT/dz and S_b and assuming constant $c_{p,l}$ for FC-72 yields

$$\begin{aligned} \frac{2c_{p,l} R dT_d(t)}{3 dt} + 2[c_{p,l} T_d(t) - (c_{p,l} T_{ini} + L)] \frac{dR}{dt} \\ = \lambda_v \frac{T_o - T_d(t)}{\rho_l \delta} (1 - \cos \theta). \end{aligned} \tag{17}$$

Substituting the equations

$$\begin{aligned} R = R_{ini} \left(1 - \frac{t}{\tau} \right)^n, \quad \frac{dR}{dt} = \frac{-nR_{ini}}{\tau} \left(1 - \frac{t}{\tau} \right)^{n-1}, \\ 1 - \cos \theta \approx \frac{\theta^2}{2} \text{ for small } \theta, \end{aligned} \tag{18}$$

and Eq. (15) for δ into Eq. (17) yields

$$\begin{aligned} A \left(1 - \frac{t}{\tau} \right) \frac{dT_d(t)}{dt} - B \left(1 - \frac{t}{\tau} \right)^{1-3n/4} \\ \times [T_o - T_d(t)]^{3/4} - CT_d(t) + D = 0, \end{aligned} \tag{19}$$

$$A = \frac{2c_{p,l} R_{ini}}{3}, \quad B = \left(\frac{\rho_v \lambda_v^3 L R_{ini} g^2}{36 \sigma_o \rho_l^3 \mu_v} \right)^{1/4}, \tag{20}$$

$$C = \frac{2nc_{p,l} R_{ini}}{\tau}, \quad D = \frac{2nR_{ini}}{\tau} (c_{p,l} T_{ini} + L).$$

This equation is solved by applying the method iteration⁵⁶ starting from the initial condition $t = 0$, $T_d = T_{ini}$. The solution of Eq. (20) depends on the experimentally determined exponent n and the characteristic time τ . Our theoretical analysis presents a new method using the measured droplet sizes to predict droplet temperatures.

C. Thermal non-equilibrium droplet evaporation

For droplet levitating on a rigid surface, the vapor lay thickness can be measured by the laser induced interference technique coupled with a high-speed-camera.⁵⁷ For droplet floating on a soft surface, such a technique is difficult to be fulfilled due to the laser dispersion caused by the liquid surface disturbance. Another issue is the blind area of the camera below the droplet base.⁵⁸ Bianc et al.²⁵ deduced that $\delta \sim R^{4/3}$ but did not consider mass loss in the upper droplet region and surface deformation of the bath. Gauthier et al.⁵³ derived $\delta \sim R^{1/4}$ by applying lubrication flow theory in the vapor film. Figures 8(a) and 8(b) present the predicted δ using the two expressions for our experiments, in which droplet radius R at time t come from our measurement. Here, to deduce δ , we consider a deformed oil surface for droplet levitation and energy dissipation via the upper-droplet region. The combination of the first two terms on the right-hand side of Eq. (15) indicates that δ depends on the oil surface tension. Oil viscosities affect δ because $\delta \sim R^{7/4}$. Droplet evaporation accelerates when using lower oil viscosities [see Fig. 4(c)]. However, Figs. 8(a) and 8(b) present the intercrossing curves of δ with the two oil viscosities of $\mu_o = 0.0480$ and 0.0965 Pa s, which is inconsistent with our measurements shown

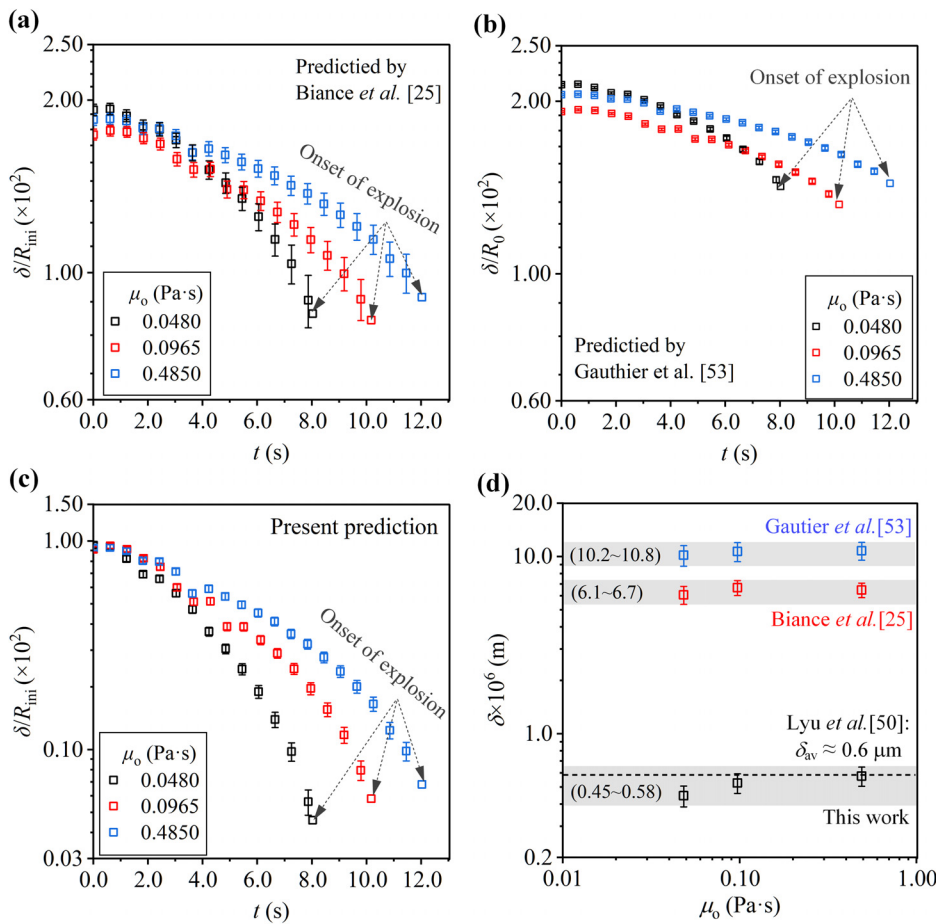


FIG. 8. Predictions of vapor-layer thicknesses. (a) Predictions by Bianco *et al.*,²⁵ (b) predictions by Gauthier *et al.*,⁵³ (c) predictions by the present authors, and (d) comparisons between different authors. All the predictions are performed with the oil superheating of $\Delta T_{\text{sat}} = 30.0^\circ\text{C}$.

in Fig. 4(c). Our predicted δ gives the correct trend for oil viscosity [see Fig. 8(c)]. A lower oil viscosity leads to a thinner vapor layer, which is consistent with the accelerating evaporation shown in Fig. 4(c).

Evidenced by larger δ predicted by Bianco *et al.*²⁵ and Gauthier *et al.*⁵³ than our present predictions, vapor layer thickness is overpredicted to underpredict droplet evaporation rate in the literature. Recall that each Leidenfrost droplet evaporation case terminates in a contact-induced explosion when the droplet radius $R = 136, 161,$ or $179 \mu\text{m}$, which corresponds to the three oil samples with $\mu_o = 0.0480, 0.0965,$ and $0.485 \text{ Pa}\cdot\text{s}$ when the oil is superheated by 30.0°C . The model of Bianco *et al.*²⁵ and Gauthier *et al.*⁵³ predicts $\delta \approx 6$ and $10 \mu\text{m}$, respectively [see Fig. 8(d)]. Our model predicts a much thinner vapor layer of $\delta \approx 0.5 \mu\text{m}$ at the termination state. This estimation, however, matches the experiment by Lyu *et al.*,⁵⁰ which found that the final-stage explosion occurs at a vapor layer of approximately $1 \mu\text{m}$, independent of droplet contamination.

Figure 9(a) presents transient droplet temperatures for $\mu_o = 0.0965 \text{ Pa}\cdot\text{s}$. The predicted values are consistent with the measured values with a maximum difference less than 1.5°C . The temperatures vary nonmonotonically, which does not support the assumption of a saturation temperature. Other oil viscosities display similar distributions. Using three oil superheating temperatures, three types of

temperature curves are detected: (I) subcooled evaporation with $\Delta T_{\text{sat}} = 14.8^\circ\text{C}$, (II) critical condition to reach saturation temperature with $\Delta T_{\text{sat}} = 23.2^\circ\text{C}$, and (III) mixed subcooled evaporation and superheated evaporation with $\Delta T_{\text{sat}} = 30.0^\circ\text{C}$. The subcooled evaporation sustains a colder droplet floating on a lower-temperature liquid bath, which, due to its longer lifetime, is attractive for applications such as self-propelled droplets. The mixed mode presents a consecutively subcooled state and a superheating state. In all three modes, droplet evaporation occurs at a temperature that clearly deviates from the saturation condition, which herein is called the “thermal non-equilibrium effect” of the Leidenfrost phenomenon.

This result of non-equilibrium evaporation inspires us to consider the internal energy of the droplet, which is written as $\tilde{E} = mc_{p,l}(T_d - T_{ini})$, referenced to initial droplet temperature T_{ini} . The sensible heat is

$$Q_{\text{ses}} = \frac{d\tilde{E}}{dt} = \frac{d[mc_{p,l}(T_d - T_{ini})]}{dt}. \quad (21)$$

The nonmonotonic variation of droplet temperatures is caused by the sensible heat absorption for $t < 2.2$ s, and sensible heat release for $t > 2.2$ s [see Fig. 9(b)]. The sensible heat release is maximal at $t = 4.4$ – 4.6 s, coinciding with the maximum temperature occurring at $t = 4.3$ – 4.7 s. Beyond the peak point, droplet temperatures decrease

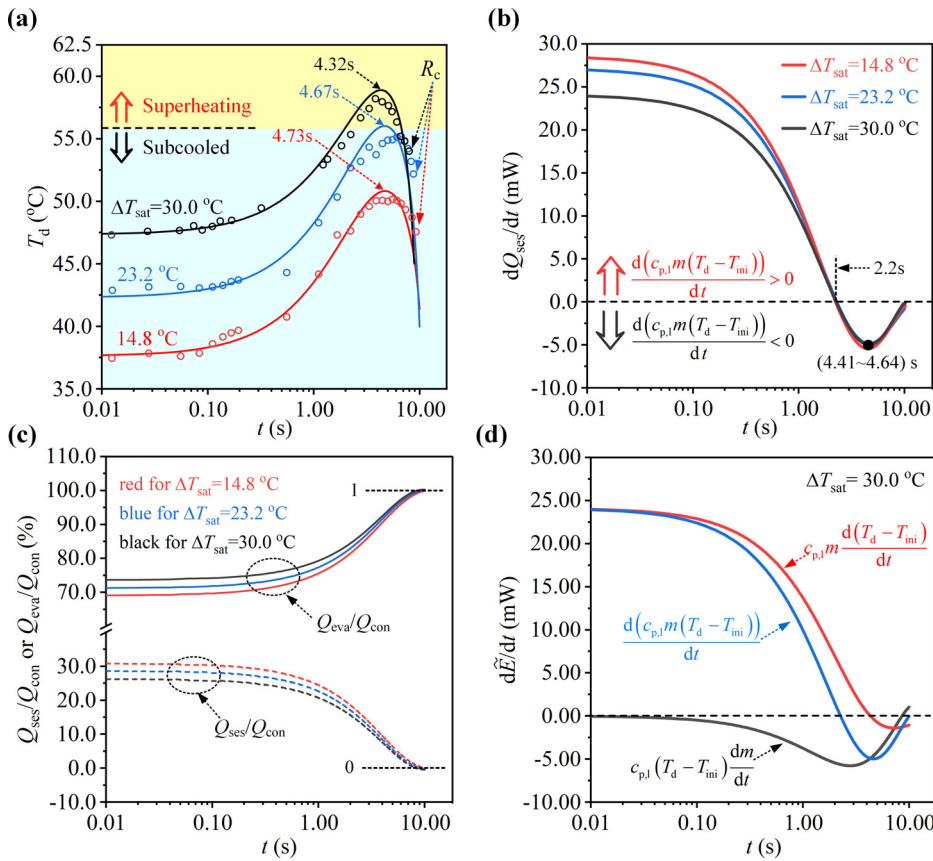


FIG. 9. Thermal non-equilibrium effect for droplet evaporation floating on liquid bath. (a) The predicted and measured droplet temperatures vs time with $\mu_o = 0.0965$ Pa s. (b) Sensible heat effect during droplet evaporation. R_c is the critical droplet radius beyond, which the IR camera gives a false temperature measurement. (c) Fraction of the evaporation heat and sensible heat to total energy received from oil. (d) Sensible heat is decoupled into temperature-variation component and mass-loss induced component.

sharply due to enhanced diffusion-controlled mass transfer in the upper region for smaller droplets. The conduction heat transfer Q_{con} across the vapor film supplies the energy Q_{eva} for droplet evaporation and the sensible heat Q_{ses} . Figure 9(c) shows that the evaporation heat and sensible heat account for about 70% and 30%, respectively, of the total energy received from oil in the earlier stage for $t < 1$ s, indicating that, indeed, the sensible heat absorption cannot be neglected, especially in the earlier stage. The sensible heat absorption quickly decreases beyond $t > 1$ s. Thus, in the later stage at $t \approx 10$ s, the thermal energy supplied from oil contributes completely to the evaporation, so the variation in sensible heat can be neglected.

Note that the sensible heat can be decoupled into two terms. Rewriting Eq. (21) yields

$$Q_{ses} = \frac{d[mc_{p,l}(T_d - T_{ini})]}{dt} = mc_{p,l} \frac{d(T_d - T_{ini})}{dt} + c_{p,l}(T_d - T_{ini}) \frac{dm}{dt}. \quad (22)$$

The first and second terms on the right-hand side of Eq. (22) are called the temperature-variation-induced sensible heat and the mass-loss-induced sensible heat. The first term can be positive or negative, depending on whether the temperature increases or decreases. However, the second term is always negative for droplet evaporation [see Fig. 9(d)]. In the very early stage such as $t < 0.2$ s, the temperature variation dominates the sensible heat. However, in the later stage such

as $t > 4$ s, the mass-loss-induced component dominates the sensible heat. The sharp temperature decrease for $t > 4.3$ – 4.7 s shown in Fig. 9(a) is mostly due to the mass-loss effect, which is identified as evaporative cooling in Refs. 23 and 59.

Figure 10 compares the measured droplet temperatures and our model predictions. Each data point represents an evaporation case, in which the maximum droplet temperature $T_{d,max}$ is recorded during the evaporation history. With R_{ini} varied from 0.6 to 0.8 mm, both measured and predicted $T_{d,max}$ is higher than the saturation temperature of FC-72, 56.6°C , indicating the droplet superheating. The model predictions well matched the measured values, with the maximum difference smaller than 0.9°C . We note that each case is repeated by three times; hence, three data points are plotted for each R_{ini} in Fig. 10. The maximum deviation among the three tests is $\sim 0.6^\circ\text{C}$ for $T_{d,max}$, indicating reliable test set-up built in this study. R_{ini} has apparent influence on $T_{d,max}$. The thermal non-equilibrium effect becomes stronger for larger R_{ini} , which is explained by smaller surface to volume ratio to weaken the heat transfer from droplet to environment at larger droplet size.

Finally, three critical phenomena are summarized here. The first is the critical transition oil superheating, beyond which Leidenfrost droplet evaporation takes place instead of droplet sinking (see Fig. 4). For $\mu_o = 0.048$ Pa s, the critical superheating temperature is approximately 10°C . The second critical phenomenon is the existence of a critical droplet radius below which the IR camera gives a false signal.

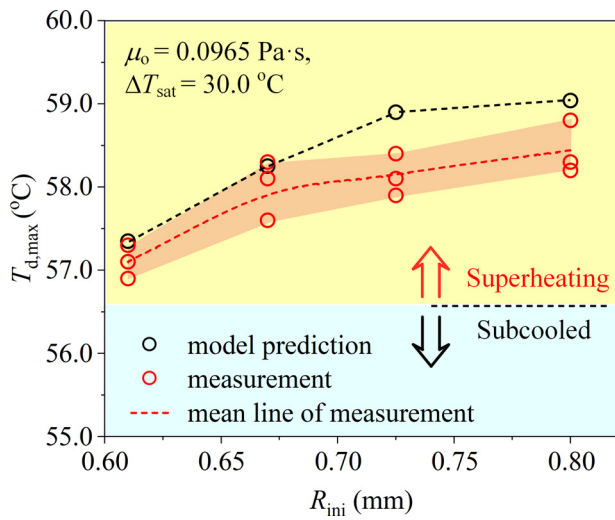


FIG. 10. Comparison of droplet temperatures between measurements and model predictions.

This radius is marked as R_c in Fig. 9(a). For droplet-temperature measurements, the IR camera captures the temperature information from a thin layer (approximately $300\ \mu\text{m}$ thick) starting from the gas–liquid interface and extending into the droplet.⁴⁴ Thus, the $300\ \mu\text{m}$ layer is called the critical optical length for IR temperature measurements and is equivalent to $2R_c$. In other words, correctly measuring the droplet temperature with the IR camera is difficult when R_c is less than about $150\ \mu\text{m}$ [an incorrectly and sharply rising droplet temperature was recorded near the end of evaporation but is not shown in Fig. 9(a)]. The third critical phenomenon is contact-boiling-induced explosion, which occurs at a smaller droplet radius $R = 130\text{--}180\ \mu\text{m}$; see comments in Secs. III A and III B.

The present paper clarifies the thermal non-equilibrium effect during droplet evaporation. Droplet temperature is a key parameter to influence droplet dynamics and evaporation rate. The droplet involves a coupled heat and mass transfer process. The droplet temperature dominates the temperature difference from liquid bath to droplet as well as from droplet to environment. Thus, the evaporation rate and the lifetime of the droplet is influenced by the droplet temperature. Droplet temperatures also influence the Marangoni flow intensity inside the droplet; thus, the temperature uniformity of the droplet is influenced by the droplet temperatures. Because temperatures and sizes of droplets are coupled with each other, the droplet temperatures also influence the force balance to affect the droplet dynamics. It is noted that the present paper focusses on the investigation of droplet evaporation floating on the oil surface. As discussed in the Introduction, the thermal non-equilibrium effect also exists for droplet evaporation levitating on the rigid surface. The droplet temperatures are either not constant vs time^{30,32} or deviate from the saturation temperature.^{31,33} This is due to the fact that the droplet evaporations on the rigid surface and the soft liquid surface have common feature of the vapor layer beneath the droplet.

IV. CONCLUSIONS

For Leidenfrost droplet evaporation on soft liquid bath, how droplet sizes and temperatures are changed vs time are important to

understand the undying mechanisms and dominate the flow and heat transfer performance. In the present work, we demonstrate that, beyond a specific oil superheating, Leidenfrost droplets evaporate in three stages: droplet oscillations, steady evaporation, and contact-boiling-induced explosion. The droplet radius follows the power law $R(t) \sim (1 - t/\tau)^n$. The results indicate that τ depends on oil viscosity and oil superheating, but n depends on oil superheating only. The exponent n decreases from 0.91 to 0.63 by increasing ΔT_{sat} from 14.8 to 70.0 °C.

Our experiment indicates that the droplet temperature varies nonmonotonically, which departs from the saturation temperature assumption for Leidenfrost droplet evaporation. For lower oil superheating, a cold (subcooled) droplet can sustain evaporation until it disappears. For larger oil superheating, both the subcooled and superheating stages occur within the droplet residence time. This non-equilibrium effect is well explained by sensible heat absorption and release. We conclude that the saturation temperature hypothesis is not always valid. A theoretical model is developed to predict droplet temperatures based on the experimentally determined characteristic time of droplet and exponent n . Our work is of interest for applications such as drug-delivery, whereby a cold droplet can float on a liquid bath, preventing the biological sample from being damaged by high temperatures and extending the droplet lifetime due to the low temperature system used.

ACKNOWLEDGMENTS

The authors acknowledge the support from the National Natural Science Foundation of China (Grant Nos. 52130608 and 52176153) and the Key Laboratories for National Defense Science and Technology (Grant No. 2021MS013).

AUTHOR DECLARATIONS

Conflict of Interest

The authors have no conflicts to disclose.

Author Contributions

Hao Wang: Data curation (lead); Formal analysis (lead); Methodology (lead); Writing – original draft (lead). **Jinliang Xu:** Conceptualization (lead); Funding acquisition (lead); Resources (lead); Supervision (lead); Writing – review & editing (lead). **Xiaoqing Ma:** Investigation (equal); Validation (equal). **Jian Xie:** Supervision (equal); Validation (equal).

DATA AVAILABILITY

The data that support the findings of this study are available from the corresponding author upon reasonable request.

NOMENCLATURE

Symbols

A, B, C, D	Four coefficients defined in Fig. 7
Bi	Biot number
$c_{p,l}$	Specific heat of liquid, $J/(kg\ K)$
D	Droplet diameter, m
\tilde{E}	Internal energy of droplet, J

g	Gravity acceleration, m/s^2
L	Latent heat of evaporation, J/kg
l	Capillary length, m
m	Mass, kg
Ma	Marangoni number
n	Exponent
P	Lifting force supplied by vapor layer to droplet, N
p	Pressure, Pa
p_a	Atmospheric pressure, Pa
Q	Quantity of heat, J
q	Volume flow rate, m^3/s
R	Droplet radius, m
R_d	Maximum “contact” radius of droplet above oil surface, m
s	The ratio of $q_{v,b}$ relative to total volume flow rate q_v
S_b	Contact area between droplet and vapor layer, m^2
T	Temperature, $^\circ\text{C}$
t	Time, s
ΔT	Temperature difference, $^\circ\text{C}$
Δt	Time step, s
u	Vapor velocity defined in Fig. 7, m/s
r	Radial coordinate along the stretched flat oil surface, m
z	Vertical coordinate normal to oil surface, m

Greek symbols

δ	Vapor layer thickness, m
δ_b	Boundary layer thickness, m
θ	Angle defined in Fig. 7
λ	Thermal conductivity, $\text{W}/(\text{m}^2 \text{K})$
μ	Viscosity, Pa s
ρ	Density, kg/m^3
σ	Surface tension, N/m
τ	Droplet characteristic lifetime, s
τ_r	Residence time of droplet, s

Subscripts

ave	Average
b	Bottom
c	Critical
con	Conduction
d	Droplet
eva	Latent heat of evaporation, J/kg
f	Fitting
l	Liquid (FC-72)
max	Maximum
o	Oil
sat	Saturation state
ses	Sensible heat
v	Vapor
ini	Initial condition

REFERENCES

- C. L. Cao, X. J. Ma, X. T. He, J. L. Xu, J. Xie, and G. H. Liu, “Self-activated elastocapillary wave promotes boiling heat transfer on soft liquid metal surface,” *Int. Commun. Heat Mass Transfer* **120**, 105019 (2021).
- A. Gauthier, G. Lajoinie, J. H. Snoeijer, and D. van der Meer, “Inverse Leidenfrost drop manipulation using menisci,” *Soft Matter* **16**, 4043 (2020).
- D. Liu and T. Tran, “Vapor-induced attraction of floating droplets,” *J. Phys. Chem. Lett.* **9**, 4771 (2018).
- C. Kleinstreuer and Z. Zhang, “Airflow and particle transport in the human respiratory system,” *Annu. Rev. Fluid Mech.* **42**, 301 (2010).
- R. Abdelaziz, D. Disci-Zayed, M. K. Hedayati, J. H. Pohls, A. U. Zillohu, B. Erkartal, V. S. Chakravadhanula, V. Duppel, L. Kienle, and M. Elbahri, “Green chemistry and nanofabrication in a levitated Leidenfrost drop,” *Nat. Commun.* **4**, 2400 (2013).
- M. Shi, J. Qiu, S. Feng, L. Zhang, Y. Zhao, T. J. Lu, and F. Xu, “Janus vitrification of droplet via cold Leidenfrost phenomenon,” *Small* **17**, e2007325 (2021).
- A. Gauthier, D. van der Meer, J. H. Snoeijer, and G. Lajoinie, “Capillary orbits,” *Nat. Commun.* **10**, 3947 (2019).
- M. Shi, F. Frank, L. T. Wang, F. Xu, T. J. Lu, and C. P. Grigoropoulos, “Role of Jakob number in Leidenfrost phenomena unveiled by theoretical modeling,” *Phys. Fluids* **31**, 042109 (2019).
- R. M. Bain, C. J. Pulliam, F. Thery, and R. G. Cooks, “Accelerated chemical reactions and organic synthesis in Leidenfrost droplets,” *Angew. Chem., Int. Ed.* **55**, 10478 (2016).
- B. Sobac, L. Maquet, A. Duchesne, H. Machrafi, A. Rednikov, P. Dauby, P. Colinet, and S. Dorbolo, “Self-induced flows enhance the levitation of Leidenfrost drops on liquid baths,” *Phys. Rev. Fluids* **5**, 062701 (2020).
- Y. Couder, E. Fort, C. H. Gautier, and A. Boudaoud, “From bouncing to floating: Noncoalescence of drops on a fluid bath,” *Phys. Rev. Lett.* **94**, 177801 (2005).
- D. Quéré, “Leidenfrost dynamics,” *Annu. Rev. Fluid Mech.* **45**, 197 (2013).
- G. Graeber, K. Regulagadda, P. Hodel, C. Kuttel, D. Landolf, T. M. Schutzius, and D. Poulikakos, “Leidenfrost droplet trampolining,” *Nat. Commun.* **12**, 1727 (2021).
- F. Celestini, T. Frisch, and Y. Pomeau, “Take off of small Leidenfrost droplets,” *Phys. Rev. Lett.* **109**, 034501 (2012).
- C. L. Cao, X. J. Ma, J. L. Xu, H. W. Li, and G. L. Liu, “Explosive boiling induced fast transportation of Leidenfrost droplet to target location,” *Phys. Fluids* **34**, 053322 (2022).
- X. J. Yu, Y. Zhang, R. Hu, and X. B. Luo, “Water droplet bouncing dynamics,” *Nano Energy* **81**, 105647 (2021).
- A. Bouillant, T. Mouterde, P. Bourriane, A. Lagarde, C. Clanet, and D. Quéré, “Leidenfrost wheels,” *Nat. Phys.* **14**, 1188 (2018).
- J. Li, X. Zhou, Y. Zhang, C. Hao, F. Zhao, M. Li, H. Tang, W. Ye, and Z. Wang, “Rectification of mobile Leidenfrost droplets by planar ratchets,” *Small* **16**, e1901751 (2020).
- H. Linke, B. J. Aleman, L. D. Melling, M. J. Taormina, M. J. Francis, C. C. Dow-Hygelund, V. Narayanan, R. P. Taylor, and A. Stout, “Self-propelled Leidenfrost droplets,” *Phys. Rev. Lett.* **96**, 154502 (2006).
- G. Lagubeau, M. L. Merrer, C. Clanet, and D. Quéré, “Leidenfrost on a ratchet,” *Nat. Phys.* **7**, 395 (2011).
- A. Askounis, Y. Kita, M. Kohno, Y. Takata, V. Koutsos, and K. Sefiane, “Influence of local heating on Marangoni flows and evaporation kinetics of pure water drops,” *Langmuir* **33**, 5666 (2017).
- D. Mamalis, V. Koutsos, and K. Sefiane, “Nonisothermal spreading dynamics of self-rewetting droplets,” *Langmuir* **34**, 1916 (2018).
- G. J. Dunn, S. K. Wilson, B. R. Duffy, S. David, and K. Sefiane, “The strong influence of substrate conductivity on droplet evaporation,” *J. Fluid Mech.* **623**, 329 (2009).
- V. S. Ajaev and O. A. Kabov, “Levitation and self-organization of droplets,” *Annu. Rev. Fluid Mech.* **53**, 203 (2021).
- A.-L. Biance, C. Clanet, and D. Quéré, “Leidenfrost drops,” *Phys. Fluids* **15**, 1632 (2003).
- L. Maquet, B. Sobac, B. Darbois-Textier, A. Duchesne, M. Brandenbourger, A. Rednikov, P. Colinet, and S. Dorbolo, “Leidenfrost drops on a heated liquid pool,” *Phys. Rev. Fluids* **1**, 053902 (2016).
- C. Cai, I. Mudawar, H. Liu, and C. Si, “Theoretical Leidenfrost point (LFP) model for sessile droplet,” *Int. J. Heat Mass Transfer* **146**, 118802 (2020).
- S. D. Janssens, S. Koizumi, and E. Fried, “Behavior of self-propelled acetone droplets in a Leidenfrost state on liquid substrates,” *Phys. Fluids* **29**, 032103 (2017).
- Y. J. Ding and J. Liu, “Dynamic interactions of Leidenfrost droplets on liquid metal surface,” *Appl. Phys. Lett.* **109**, 121904 (2016).

- ³⁰T. Orzechowski and S. Wcislik, "Instantaneous heat transfer for large drops levitating over a hot surface," *Int. J. Heat Mass Transfer* **73**, 110 (2014).
- ³¹E. Yim, A. Bouilliant, D. Quéré, and F. Gallaire, "Stability of Leidenfrost drops inner flows," [arXiv:2012.10408](https://arxiv.org/abs/2012.10408) (2020).
- ³²E. Mogilevskiy, "Levitation of a nonboiling droplet over hot liquid bath," *Phys. Fluids* **32**, 012114 (2020).
- ³³G. Castanet, O. Caballina, W. Chaze, R. Collignon, and F. Lemoine, "The Leidenfrost transition of water droplets impinging onto a superheated surface," *Int. J. Heat Mass Transfer* **160**, 120126 (2020).
- ³⁴A. M. Cazabat and G. Guena, "Evaporation of macroscopic sessile droplets," *Soft Matter* **6**, 2591 (2010).
- ³⁵C. Poulard, G. Guéna, and A. M. Cazabat, "Diffusion-driven evaporation of sessile drops," *J. Phys.: Condens. Matter* **17**, S4213 (2005).
- ³⁶R. G. Larson, "Transport and deposition patterns in drying sessile droplets," *AIChE J.* **60**, 1538 (2014).
- ³⁷H. Kim and N. Sung, "The effect of ambient pressure on the evaporation of a single droplet and a spray," *Combust. Flame* **135**, 261 (2003).
- ³⁸B. Sobac and D. Brutin, "Triple-line behavior and wettability controlled by nanostructured substrates: Influence on sessile drop evaporation," *Langmuir* **27**, 14999 (2011).
- ³⁹N. M. Kovalchuk, A. Trybala, and V. M. Starov, "Evaporation of sessile droplets," *Curr. Opin. Colloid Interface Sci.* **19**, 336 (2014).
- ⁴⁰B. S. Gottfried, C. J. Lee, and K. J. Bell, "The Leidenfrost phenomenon: Film boiling of liquid droplets on a flat plate," *Int. J. Heat Mass Transfer* **9**, 1167 (1966).
- ⁴¹A. L. N. Moreira, A. S. Moita, and M. R. Panão, "Advances and challenges in explaining fuel spray impingement: How much of single droplet impact research is useful?," *Prog. Energy Combust. Sci.* **36**, 554 (2010).
- ⁴²T. Tran, H. J. Staat, A. Prosperetti, C. Sun, and D. Lohse, "Drop impact on superheated surfaces," *Phys. Rev. Lett.* **108**, 036101 (2012).
- ⁴³J. L. Xu, X. Yan, G. H. Liu, and J. Xie, "The critical nanofluid concentration as the crossover between changed and unchanged solar-driven droplet evaporation rates," *Nano Energy* **57**, 791 (2019).
- ⁴⁴X. Yan, J. Xu, Z. Meng, J. Xie, and G. Liu, "Multiscale characteristic in symmetric/asymmetric solar-driven nanofluid droplet evaporation," *Langmuir* **36**, 1680 (2020).
- ⁴⁵T. L. Bergman, T. L. Bergman, F. P. Incropera, D. P. Dewitt, and A. S. Lavine, *Fundamentals of Heat and Mass Transfer* (John Wiley & Sons, 2011).
- ⁴⁶H. W. Coleman and W. G. Steele, *Experimentation, Validation, and Uncertainty Analysis for Engineers* (Wiley, 2018).
- ⁴⁷J. Zawala, S. Dorbolo, D. Terwagne, N. Vandewalle, and K. Malysa, "Bouncing bubble on a liquid/gas interface resting or vibrating," *Soft Matter* **7**, 6719 (2011).
- ⁴⁸J. Kamp, J. Villwock, and M. Kraume, "Drop coalescence in technical liquid/liquid applications: A review on experimental techniques and modeling approaches," *Rev. Chem. Eng.* **33**, 1 (2017).
- ⁴⁹R. Savino, D. Paterna, and M. Lappa, "Marangoni flotation of liquid droplets," *J. Fluid Mech.* **479**, 307 (2003).
- ⁵⁰S. Lyu, V. Mathai, Y. Wang, B. Sobac, P. Colinet, D. Lohse, and C. Sun, "Final fate of a Leidenfrost droplet: Explosion or takeoff," *Sci. Adv.* **5**, eaav8081 (2019).
- ⁵¹J. D. Bernardin and I. Mudawar, "The Leidenfrost point: Experimental study and assessment of existing models," *J. Heat Transfer* **121**, 894 (1999).
- ⁵²T. G. Myers and J. P. F. Charpin, "A mathematical model of the Leidenfrost effect on an axisymmetric droplet," *Phys. Fluids* **21**, 063101 (2009).
- ⁵³A. Gauthier, C. Diddens, R. Proville, D. Lohse, and D. van der Meer, "Self-propulsion of inverse Leidenfrost drops on a cryogenic bath," *Proc. Natl. Acad. Sci. U. S. A.* **116**, 1174 (2019).
- ⁵⁴B. R. Munson, T. H. Okiishi, W. W. Huebsch, and A. P. Rothmayer, *Fluid Mechanics* (Wiley, Singapore, 2013).
- ⁵⁵S. Chandra and S. D. Aziz, "Leidenfrost evaporation of liquid nitrogen droplets," *J. Heat Transfer* **116**, 999 (1994).
- ⁵⁶W. Minkowycz, *Advances in Numerical Heat Transfer* (CRC Press, 1996).
- ⁵⁷J. C. Burton, A. L. Sharpe, R. C. van der Veen, A. Franco, and S. R. Nagel, "Geometry of the vapor layer under a Leidenfrost drop," *Phys. Rev. Lett.* **109**, 074301 (2012).
- ⁵⁸M. A. J. van Limbeek, B. Sobac, A. Rednikov, P. Colinet, and J. H. Snoeijer, "Asymptotic theory for a Leidenfrost drop on a liquid pool," *J. Fluid Mech.* **863**, 1157 (2019).
- ⁵⁹Z. Pan, S. Dash, J. A. Weibel, and S. V. Garimella, "Assessment of water droplet evaporation mechanisms on hydrophobic and superhydrophobic substrates," *Langmuir* **29**, 15831 (2013).